Cellular vortex shedding in the wake of a tapered plate at low Reynolds number

Hatef A. Khaledi, Vagesh D. Narasimhamurthy, and Helge I. Andersson
Department of Energy and Process Engineering, Norwegian University of Science and Technology, 7491 Trondheim, Norway

(Received 17 June 2008; accepted 13 November 2008; published online 27 January 2009)

The unsteady near wake behind a linearly tapered plate has been investigated numerically. The tapering made the Reynolds number based on the inflow velocity and the local width of the plate vary from 25 to 100. The wake flow comprised three different flow regimes coexisting side by side. The wake flow was steady behind the narrow end of the plate. Periodic vortex shedding occurred downstream from where the local Reynolds number exceeded 32. Vortex dislocations enabled a cellular shedding pattern with shedding frequency decreasing toward the wide end of the plate. The regular oblique vortex shedding near midspan was subjected to three-dimensional scrambling toward the wide end of the plate which gave rise to streamwise-oriented vortex structures. The Strouhal number was distinctly lower than in the wake of a uniform plate whereas the base pressure coefficient was substantially higher. © *2009 American Institute of Physics*.
[DOI: 10.1063/1.3059619]

I. INTRODUCTION

Bluff-body wakes and their vortex structure have been the subject of numerous investigations partly because of the direct practical importance of integral quantities such as drag and lift coefficients but also due to their inherent complexities which continue to fascinate and challenge the research community. Flow past simple bluff bodies such as plates, circular cylinders, and tori have been pondered on more frequently due to their geometrical simplicity. A unique feature of the flow past a normal flat plate, unlike most other bluff bodies such as the circular cylinder and the sphere, is that the separation points are fixed. The wake behind the plate nevertheless shares most of the complexities of wakes of other bluff bodies. Moreover, wake instabilities and flow transition occur at substantially lower Reynolds numbers for the flat plate wake than, for instance, for a cylinder wake.

Three dimensionalizations of an originally regular two-dimensional (2D) wake can be ascribed to secondary instabilities. This takes place *intrinsically* for wakes of 2D bluff bodies at a certain critical Reynolds number and inevitably induces spanwise variations in the flow field.[1,2] Three dimensionalizations can also arise *extrinsically* if the geometry of the bluff body is tapered or otherwise asymmetric[3–5] or by manipulation of the boundary conditions.[6,7] Extrinsical three dimensionalization was first considered by Gaster[3] in an experimental study of vortex shedding behind a very slender cone. He conceived that the velocity fluctuations in the wake were not singly periodic in time but rather exhibited two different frequencies with one an order of magnitude lower than the other. This modulation frequency turned out to be constant all along the span. In a subsequent heuristic study[8] he observed a *cellular* structure of the vortex shedding behind a mildly tapered cylinder at low Reynolds numbers. Cellular vortex shedding implies that cells of different frequencies coexist along the span of the body. In the case of a tapered cylinder geometry where the diameter varies linearly, the cellular vortex structures result in "oblique" vortex shedding. Nonetheless, several investigations have reported that cellular vortex structures are not the only stimuli of oblique shedding. The actual boundary conditions at the spanwise ends may also lead to inclined vortex structures.[9,10] It is indeed likely that in the case of different coexisting cells, adjacent vortices will be out of phase with each other and spanwise vortex filaments split apart. Although such vortex dislocations were first introduced as a main feature of three-dimensional (3D) wake transitions, vortex dislocations may also occur in laminar wakes and the phenomenon is then not blurred by the turbulence.

After having observed vortex dislocations and cellular flow patterns in the wake of cones, Gaster and Ponsford[11] set up a new experiment for flow over a tapered plate at Reynolds numbers of order 10^4. They provided limited data for wakes behind plates with taper ratios (TRs) $[\equiv l/(d_2-d_1)]$ in the range $8<\mathrm{TR}<240$, where l is the length of the plate and d_2 and d_1 are the widths at wide and narrow ends, respectively. In spite of the fact that they found an evidential base pressure gradient along the span which induced a spanwise secondary flow, they failed to detect any cellular vortex pattern. This contrasted with the preceding investigation of Maull and Young[6] who observed a cellular vortex structure behind a parallel-sided (i.e., nontapered or uniform) plate in uniform shear. This contradiction motivated Castro and Rogers[12] and Castro and Watson[13] to undertake an extensive experimental investigation of the wake of tapered and triangular plates with different TRs and different end boundary conditions. The Reynolds number based on the uniform inflow velocity and the local plate width was of the order of 10^4. They observed cells with constant shedding frequency throughout the TR range of $20<\mathrm{TR}<60$. Very recently, Narasimhamurthy *et al.*[5] performed a direct numerical simu-

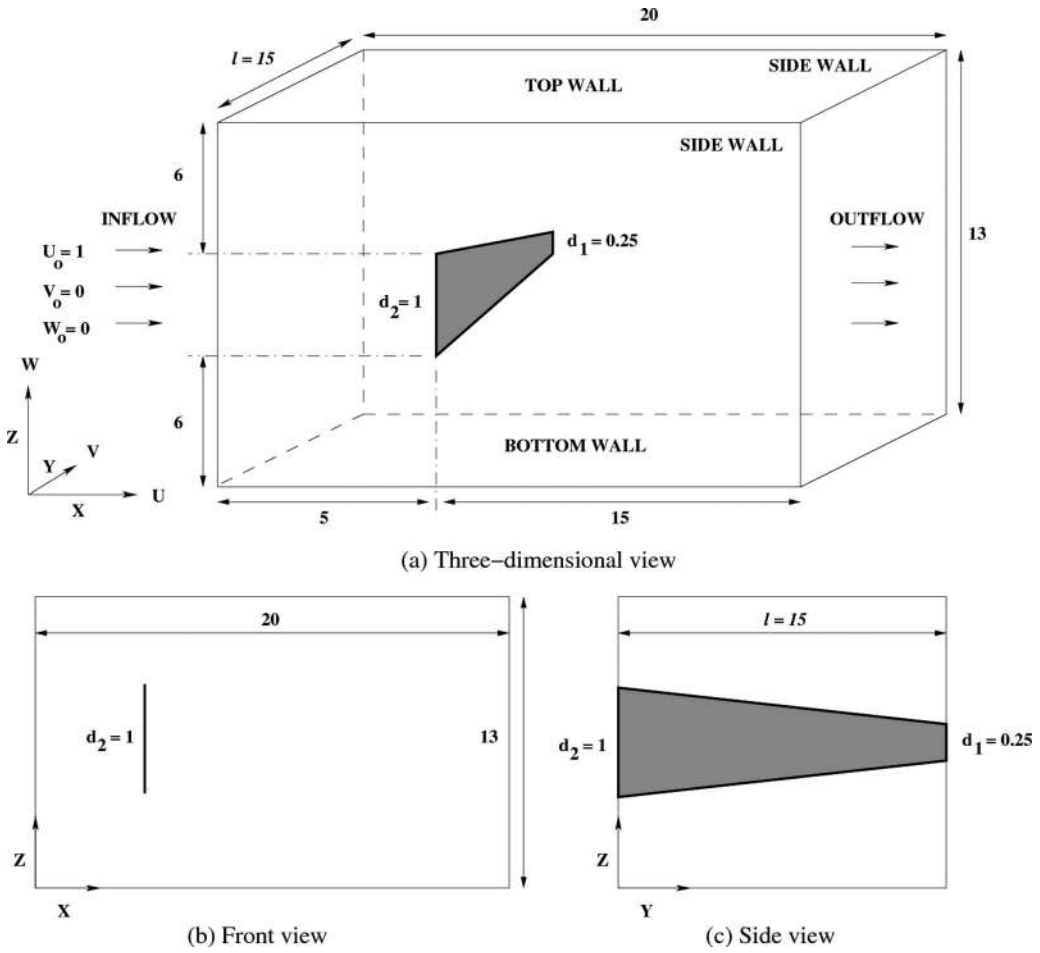

FIG. 1. Flow domain and coordinate system. All lengths are scaled with d_2.

lation of turbulent flow around a tapered plate with $250<\mathrm{Re}<1000$ and also found that the wake exhibited a cellular vortex structure.

The parallel-sided plate placed perpendicular to the incoming flow has been the eye-catcher case of several experimentalists for decades. Almost all laboratory experiments have been carried out in the turbulent regime. Fage and Johansen[14] measured the pressure upstream and downstream of the plate at various angles of attack for a Reynolds number of 1.5×10^5. Hotwire anemometry was used by Perry and Steiner[15] to study the flow past flat and inclined plates at Reynolds number 2×10^4. Castro and Jones[16] performed 2D computer simulations of steady flow in the Reynolds number range $100<\mathrm{Re}<800$ assuming symmetry about the centerline. Because of the assumptions of steady-state conditions and centerline symmetry, the wake length was substantially greater than it would be for the case when centerline symmetry is not imposed. Joshi[17] performed both 2D and 3D numerical simulations using a second-order accurate finite-volume time-splitting scheme at Reynolds numbers varying from 40 to 1000. Unsteady 2D simulations with a higher-order scheme were reported by Najjar and Vanka[18] for Reynolds numbers in the range of 80–1000. They observed parallel shedding below Re=250 whereas complex nonlinear interactions such as vortex pairing and tearing were observed in the far-wake region at higher Reynolds numbers. More recently Najjar[19] conducted 3D simulations to resolve the overprediction of the drag coefficient due to the inherent three dimensionality above Re=200. Balachandar *et al.*[20] calculated various properties of the time- and span-averaged mean-wake recirculation region in separated flows for several 2D bluff bodies at various Reynolds numbers. The parallel-sided flat plate was among the different bodies considered and the recirculation bubble length and various mean statistics were reported for Re=250. Najjar and Balachandar[21] conducted a computer experiment for a parallel-sided flat plate also at Re=250. They studied the long-time signature of the drag and lift coefficients and observed a low-frequency modulation which they interpreted as a gradual variation of the flow field between two different flow regimes. Spanwise correlation measurements in combination with smoke visualizations of vortex shedding behind a flat plate at Re=1 800 and Re=27 000 were recently performed by Wu *et al.*[22]

In comparison with the many experimental investigations of flows past uniform or tapered plates, relatively few numerical studies have so far been published. Although it is not feasible to resolve the entire range of turbulent scales at high Reynolds numbers, fully resolved time-dependent solutions of the full 3D Navier–Stokes equations at lower Reynolds numbers enable detailed explorations of bluff-body wakes both in the unsteady laminar and in the lower-Re tur-

TABLE I. Boundary conditions for the computational domain in Fig. 1.

Face	Boundary conditions
Inflow	$U_0=1$; $V_0=W_0=0$; $\partial P/\partial x=0$
Side walls	$V=0$; $\partial U/\partial Y=\partial W/\partial Y=\partial P/\partial Y=0$
Top and bottom wall	$W=0$; $\partial U/\partial Z=\partial V/\partial Z=\partial P/\partial Z=0$
Outflow	$P=0$; $\partial U/\partial X=\partial V/\partial X=\partial W/\partial X=0$

bulent flow regime. The present study is devoted to the presumably complex wake behind a tapered plate with TR=20 and with Re=25 at the narrow end and Re=100 at the wide end. The study is aimed at exploring the instantaneous flow field and vortex structures which may occur in the nominally laminar wake. It is expected that the wake structure will vary substantially along the span of the plate due to the variation of the local Reynolds number. In order to separate the Reynolds number effect from the influence of the tapering, comparisons will be drawn with results from a separate simulation of flow past a uniform (i.e., nontapered) plate at Re=62.5, corresponding to the local Reynolds number at the midspan of the tapered plate.

II. FLOW CONFIGURATION AND COMPUTATIONAL APPROACH

The incompressible flow normal to a thin flat plate is considered. The oncoming flow is homogeneous and free of disturbances. The width of the plate increases *linearly* between d_1 and d_2, where d_1 is the width of the plate at the narrow end and d_2 denotes the plate width at the wide end. The plate considered herein is $l=15d_2$ long and only $0.02d_2$ thick and $d_1=0.25d_2$. The mean width of the plate is thus $d_m=0.625d_2$, the plate aspect ratio (AR=l/d_m) is 24 and TR equals 20. The local Reynolds number $\mathrm{Re}\equiv U_0 d/\nu$ based on the uniform velocity U_0 of the oncoming flow, the local plate width d, and the kinematic fluid viscosity ν varies between 100 and 25 from the wide to the narrow end of the plate. In the following, all spatial dimensions will be nondimensionalized by d_2 and all velocities will be normalized with the uniform inflow velocity U_0, unless otherwise explicitly mentioned.

The flow is governed by the incompressible Navier–Stokes equations. The 3D momentum equations and the continuity equations are approximated on a staggered Cartesian grid system. A third-order explicit Runge–Kutta scheme in time and a second-order accurate central-differencing scheme in space are employed in combination with an iterative strongly implicit procedure for solving the Poisson equation. The simulations were run with the well-documented finite-volume solver MGLET.[23]

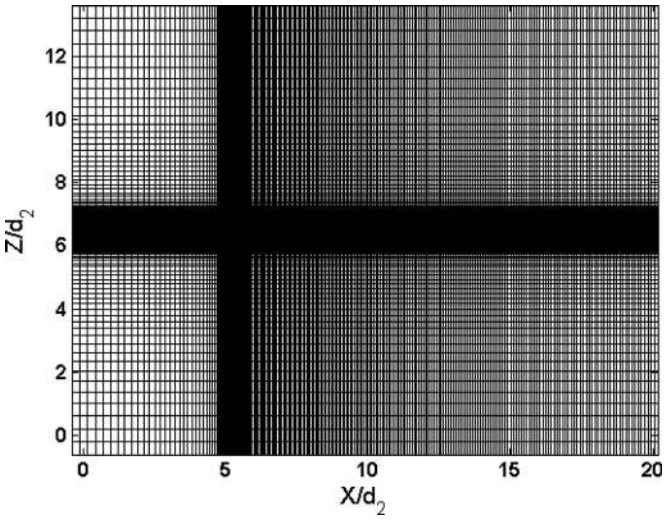

FIG. 2. The computational mesh in the (X,Z) plane for case B. The grid spacing is uniform in the spanwise Y direction. See also Table II.

The computational domain is shown in Fig. 1 whereas Table I gives an overview of the boundary conditions used. A uniform velocity profile $U_0=1$ was prescribed as inlet boundary condition together with a Neumann boundary condition for the pressure. Free-slip boundary conditions were applied at the side walls and at the top wall and bottom wall. The choice of slip rather than no-slip conditions eliminates end effects. At the outlet, the Neumann and Dirichlet boundary conditions were set for the velocity components and the pressure, respectively.

To accommodate the tapered plate in the Cartesian mesh, a direct-forcing immersed boundary method (IBM) is used. A recent review of different IBM schemes was provided by Mittal and Iaccarino.[24] A complete description of the direct-forcing method implemented in MGLET can be found in the article by Peller *et al.*[25]

In order to assure a grid-independent solution, two different grid resolutions were utilized; see Table II. The coarse grid (A) consisted of 4.2×10^6 points whereas the fine grid (B) depicted in Fig. 2 consisted of 7.2×10^6 points. In both cases the grid spacing was uniform only in the lateral Y direction. The grid cells were nonuniformly distributed in the XZ plane with a clustering around the plate and in the near wake. The smallest and largest grid spacing in the three different coordinate directions are provided in Table II. The

TABLE II. Geometrical and computational parameters. L_i and N_i denote the length of the domain and number of grid points in the X_i direction. AR and TR are the aspect ratio and taper ratio of the plate, respectively. The smallest and largest grid spacings are all normalized with d_2.

	Dimension $L_x\times L_y\times L_z$	Grid points $N_x\times N_y\times N_z$	AR	TR	Re_1	Re_2	Max. Δx	Min. Δx	Max. Δy	Min. Δy	Max. Δz	Min. Δz
Tapered A	$20\times15\times13$	$220\times125\times150$	24	20	25	100	0.279	0.01	0.12	0.12	0.625	0.0125
Tapered B	$20\times15\times13$	$258\times150\times184$	24	20	25	100	0.232	0.008	0.1	0.1	0.405	0.01
Parallel-sided plate	$20\times6\times16$	$192\times60\times192$	9.6	∞	62.5	62.5	0.24	0.01	0.1	0.1	0.12	0.05

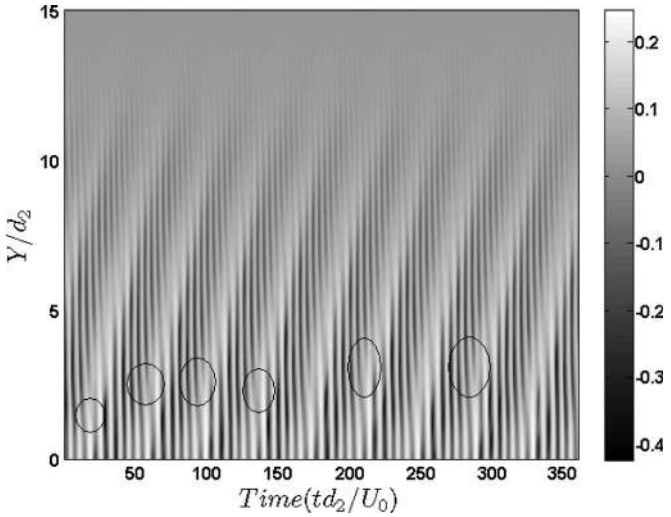

FIG. 3. Time evolution of cross-stream velocity (W) along the span. The sampling line is located at $x=4d_m$ and $z=-1d_m$ from the axis of the plate. Some vortex dislocations are encircled.

time step used was $\Delta t=0.003d_2/U_0$ and the number of Poisson iterations per time step was limited to 30.

For comparative purposes the flow past a parallel-sided (i.e., uniform) plate with constant width d equal to the mean width d_m of the tapered plate has also been simulated. In the case of a nontapered plate, periodic boundary conditions were used at the lateral sides of the computational domain. The wake behind a uniform body is homogeneous in the lateral direction and a shorter length l of the plate sufficed; see Table II. The bulk of the results presented in the following section are from the fine-grid simulation (B). Comparisons between coarse-grid and fine-grid results will be provided in Sec. III A. Comparisons between the wake flow behind tapered and nontapered plates will be made whenever relevant.

III. RESULTS AND DISCUSSIONS

A. Frequency analysis and wake pattern

All three instantaneous velocity components U, V, W and the instantaneous pressure P were sampled along two lines parallel to the axis of the plate. The sampling lines were located $4d_m$ and $7d_m$ downstream of the plate axis in the x direction and were offset $1d_m$ in the z direction from the (x-y) plane through the axis of the plate. The total sampling time was $360d_2/U_0$ (120 000 time steps) and encompassed nearly 55 shedding cycles at the wide end of the plate.

The time traces of the instantaneous cross-stream velocity (W) along the first sampling line are shown in Fig. 3. The aslant pattern of the time traces clearly demonstrates the oblique-like vortex shedding along the span. Moreover, the vortex splitting or dislocation is clearly notable. Some of these dislocations are marked in the figure by circles. The figure also reveals a periodic occurrence of the vortex dislocations at certain spanwise locations. This regularity is probably an intrinsic feature of laminar vortex shedding and contrasts with the recent observation of Narasimhamurthy *et al.*[5]

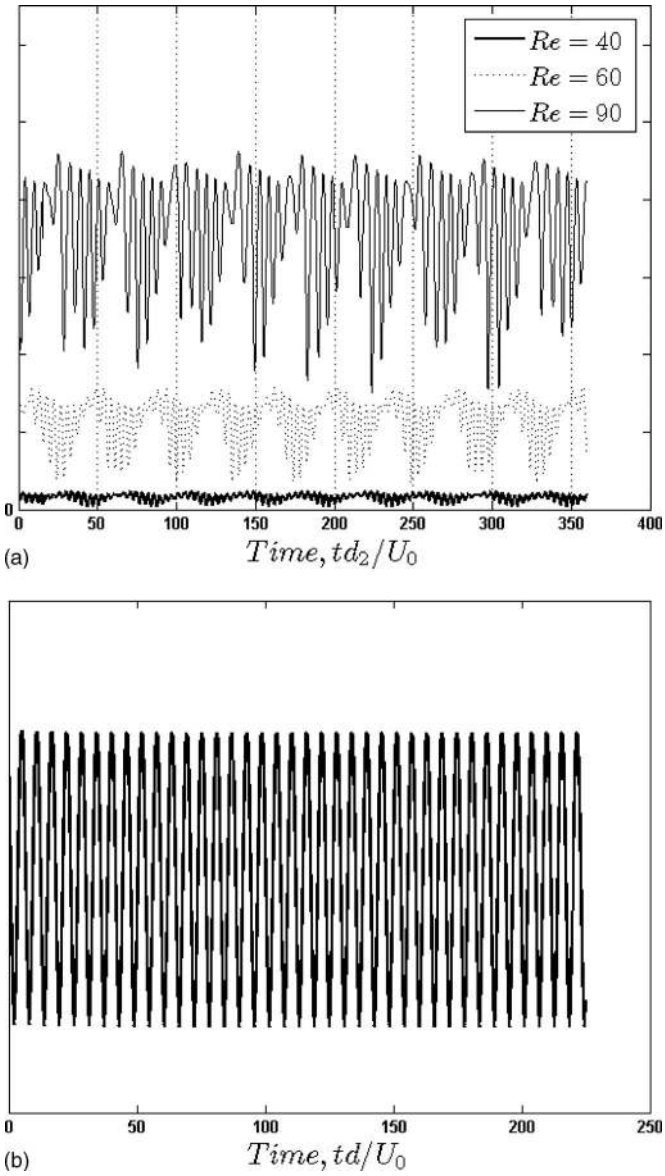

FIG. 4. (a) Time trace of the cross-stream velocity component W for the tapered plate at three local Reynolds numbers, i.e., at different spanwise locations. (b) Time trace of the cross-stream velocity W for the parallel-sided plate.

who reported random and chaotic occurrences of vortex dislocations and splitting in the turbulent wake behind a tapered plate.

Time traces of W at three different spanwise locations, i.e., for three different local Reynolds numbers, are shown in Fig. 4(a). The low-frequency, low amplitude signals that modulate the high-frequency flapping signals can be attributed to the presence of large-scale spotlike vortex dislocations that were first observed by Williamson[26] in the wake of a uniform circular cylinder. The time record for Reynolds number of 90, for instance, reveals a distinct low-frequency signature. The period of this low-frequency modulation is about $35d_2/U_0$ which is fully consistent with the separation between the circles (at about $Y/d_2 \approx 2$) in Fig. 3. This observation is in fact a strong endorsement of the claim that these low-frequency irregularities are due to vortex splitting. This

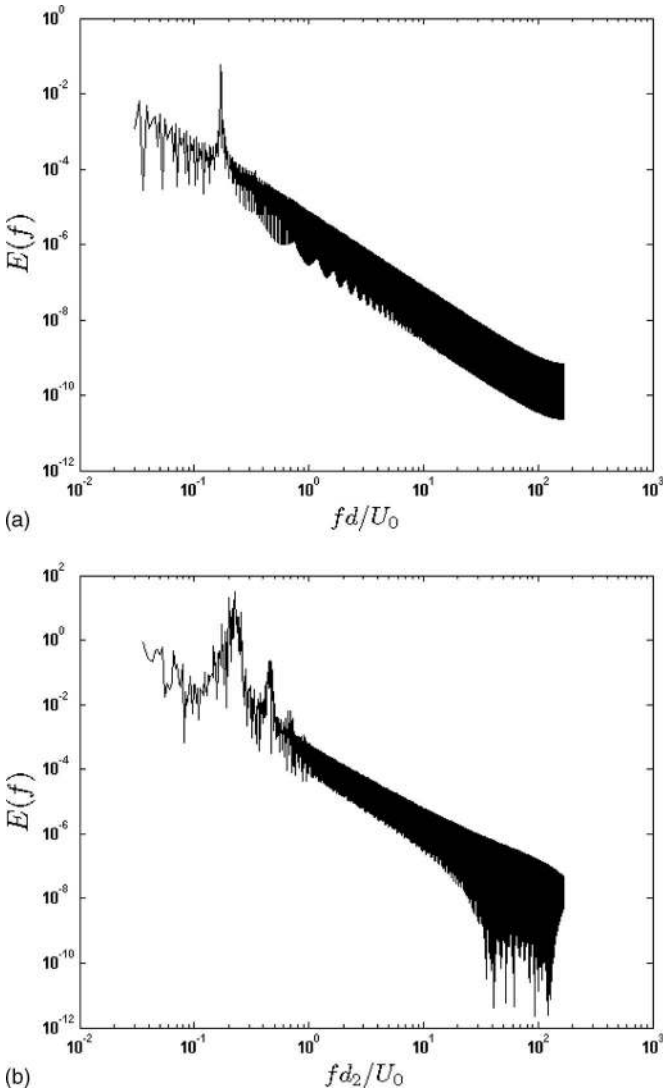

FIG. 5. One-dimensional energy spectrum: (a) parallel-sided plate (Re=62.5) and (b) tapered plate at midspan, i.e., local Re_{local}=62.5.

is, however, not always the case. Najjar and Vanka[2] conjectured that these low-frequency signals are due to oscillations of the shear-layer itself. Several other interpretations of such low-frequency modulations in the wake of a uniform plate can be found from Najjar and Balachandar[21] and Wu *et al.*[22] For the sake of comparison, a time trace of the cross-stream W velocity for a parallel-sided plate is shown in Fig. 4(b). No low-frequency modulation can be seen in this figure since the vortices shed from the uniform plate are not subjected to dislocation or splitting.

One-dimensional energy spectra for the parallel-sided plate and the tapered plate are shown in Fig. 5. The spectral estimator for a finite-length time record of the cross-stream velocity component W is

$$E(f) = \frac{\hat{W} \times \hat{W}^*}{T}. \quad (1)$$

In Eq. (1) the superscript * denotes the conjugate of the Fourier-transformed W. The dominant frequency for the parallel-sided plate corresponds to $St \equiv fd/U_0 = 0.1704$ and is associated with the primary vortex shedding. The 2D calculations by Joshi[17] for Re=100 gave Strouhal number of 0.175. Tamaddon-Jahromi *et al.*[27] obtained a Strouhal number of 0.173 for Re=126 and Najjar and Vanka[18] reported a Strouhal number of 0.166 at Re=100 from their computational study. The Strouhal number for the parallel-sided plate is thus in accordance with earlier results; see Table III.

TABLE III. Strouhal numbers in the present cases compared with data reported by others.

	Reynolds number	Strouhal number
Tapered plate, current simulation	62.5	0.1414
Parallel-sided plate, current simulation	62.5	0.1704
Parallel-sided plate, Joshi (Ref. 17)	100	0.175
Parallel-sided plate, Tamaddon-Jahromi *et al.* (Ref. 27)	126	0.173
Parallel-sided plate, Najjar and Vanka (Ref. 18)	100	0.166

The energy spectrum at midspan for the tapered plate shown in Fig. 5(b) is different from the energy spectrum for the nontapered plate in spite of the same local Reynolds number. The *local* Strouhal number ($St_{local} = fd_{local}/U_0$) associated with the most dominant frequency is 0.1414, i.e., distinctly lower than the Strouhal number for the parallel-sided plate. The same observation has already been made for circular cylinders, namely, that tapering reduces the Strouhal number as compared with a uniform cylinder wake.[3,4]

The experimental findings at higher Reynolds number[13] suggest that there can be two dominant shedding frequencies at the same location. However, this is not the case in this numerical simulation. In Fig. 5(b) where the energy spectrum of the tapered plate at local Reynolds number of 62.5 has been depicted, two peaks coexist at the same location but it is clear that the second peak is nearly an order of magnitude smaller than the biggest peak and cannot be conjectured as the second dominant shedding frequency. This second peak in the spectrum is perhaps due to a secondary instability mechanism inside the flow. The same feature can be seen in the energy spectra of other shedding locations.

The spanwise variation of the frequency spectrum of the cross-stream velocity (W) is shown in Fig. 7(a). Different dominant shedding frequencies are observed at different spanwise positions and reflect the cellular pattern of the vortex structure. This is evident from Fig. 7(b) where the local Strouhal number variation along the span of the tapered plate is shown. It should be noted that the Strouhal number does not vary continuously but rather exhibits discrete linear parts which reflect constant-frequency shedding cells. The spectral analysis shows that no regular vortex shedding occurs near the narrow end of the tapered plate where $Re_{local} \leq 32$, whereas distinct cellular shedding takes place along the remainder of the span.

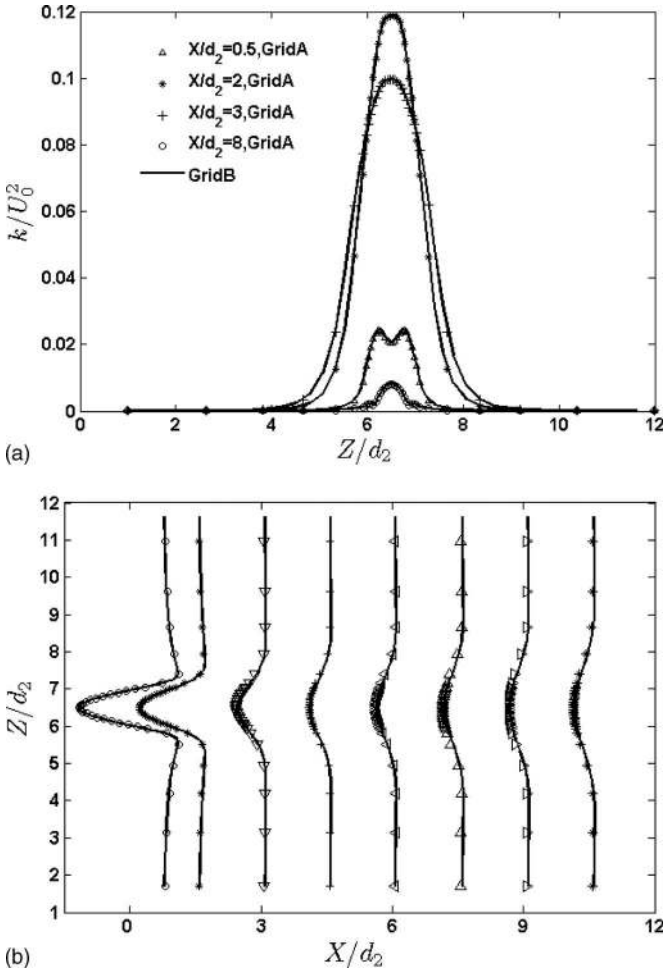

FIG. 6. Grid-independency analysis. The symbols represent results from case A and the solid lines are data from case B. X is measured from the plate. (a) Unsteady kinetic energy at different streamwise locations; (b) mean streamwise velocity $\bar{U}$ profiles.

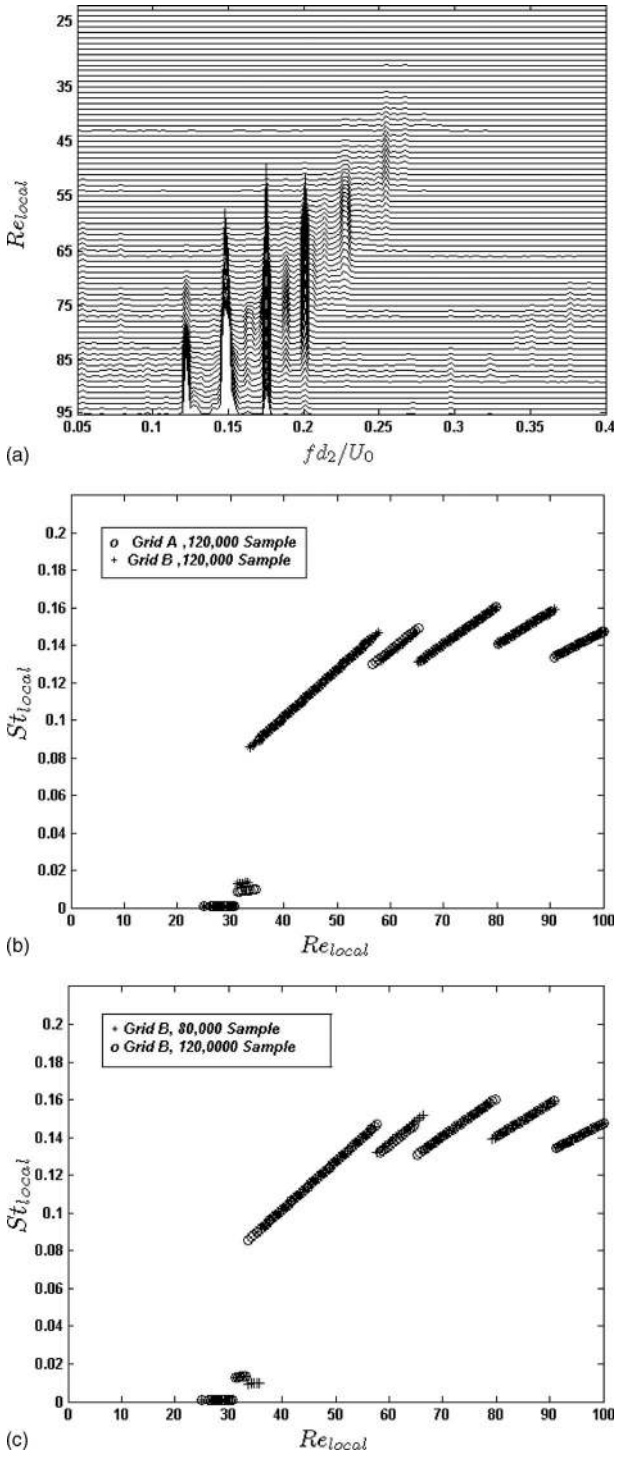

FIG. 7. (a) Spanwise variation of the frequency spectrum of the cross-stream velocity; (b) the spanwise variation of the local Strouhal number corresponding to the peak in the spectrum for two different grids; (c) the spanwise distribution of the local Strouhal number corresponding to the peak in the spectrum for two different sampling times.

Besides the discrete variation of the Strouhal number, Fig. 7(b) also compares the results of the coarse-grid (case A) and the fine-grid (case B) simulations. The results of the two simulations are practically indistinguishable. To further address the adequacy of the computational mesh, profiles of the unsteady kinetic energy k defined as $0.5\overline{u_i' u_i'}$ and mean streamwise velocity $\bar{U}$ obtained with the two different grid resolutions are compared in Fig. 6. The velocity fluctuations carry more information of the smaller temporal and spatial scales in the flow and are therefore believed to be more sensitive to the grid resolution. The close correspondence between the results of the two different simulations demonstrates the grid independency. Nonetheless, all results presented in this paper stem from the fine-grid simulation. The comparison in Fig. 7(c) between Strouhal numbers deduced after $240 d_2/U_0$ with the results after $360 d_2/U_0$ shows that the sampling time used is appropriate for the flow under consideration.

The instantaneous velocity contours at three different spanwise locations in Fig. 8 reveal that the originally steady and symmetric wake becomes unsteady at a certain spanwise location, i.e., when the local Reynolds number becomes sufficiently high. This is in keeping with Fig. 7(b), which shows that the onset of vortex shedding occurs somewhere around $\mathrm{Re}_{\mathrm{local}}=32$. While the wake is apparently symmetric at $\mathrm{Re}_{\mathrm{local}}=30$ in Fig. 8(a), a distinctly asymmetric wake can be seen at $\mathrm{Re}_{\mathrm{local}}=32$ in Fig. 8(b) and a typical alternating shed-

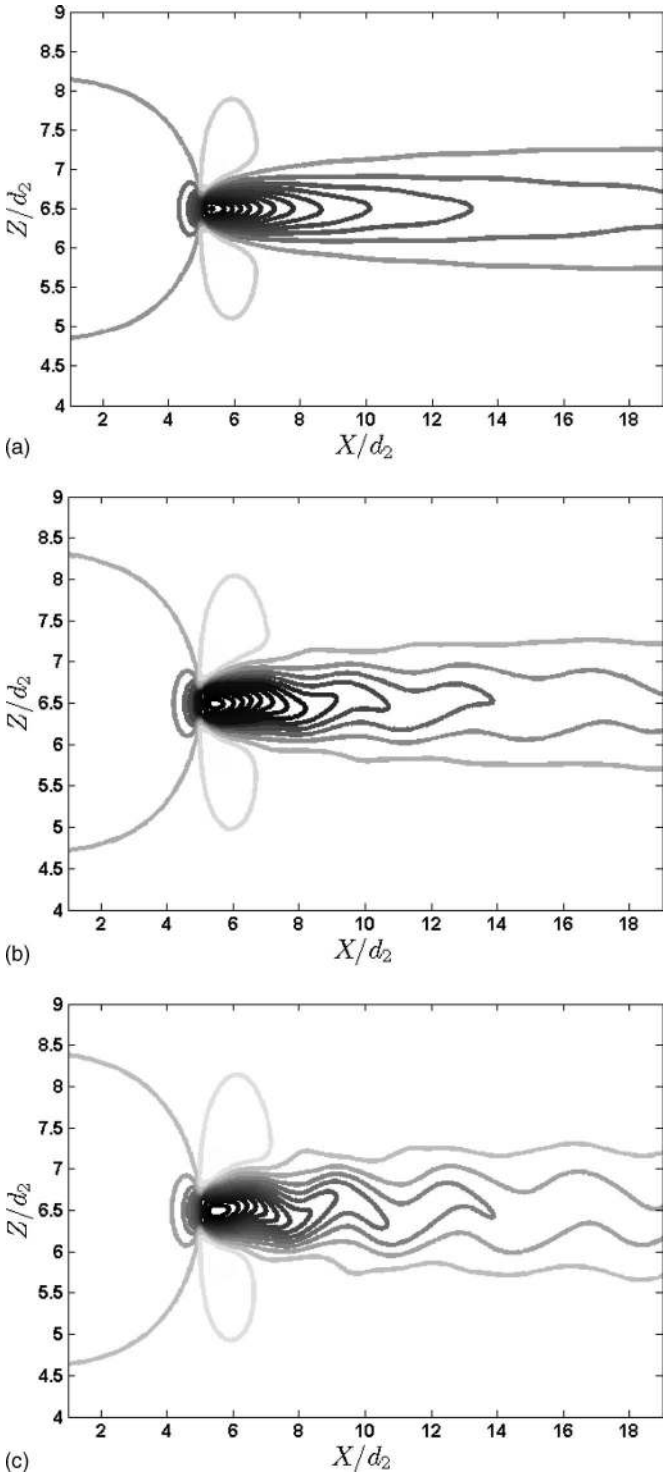

FIG. 8. Isocontour plots of the instantaneous streamwise velocity U/U_0 at three different spanwise locations. (a) $\mathrm{Re}_{\mathrm{local}}=30$, (b) $\mathrm{Re}_{\mathrm{local}}=32$, and (c) $\mathrm{Re}_{\mathrm{local}}=35$. The lines represent values between -0.2 and 1.2.

ding pattern has been established at $\mathrm{Re}_{\mathrm{local}}=35$ in Fig. 8(c). This periodic shedding of vortices at $\mathrm{Re}_{\mathrm{local}}=35$ is consistent with Fig. 7(b). The present observation is moreover in accordance with the recent finding by Saha[28] that the near wake of a parallel-sided plate becomes unsteady at a Reynolds number in between 30 and 35.

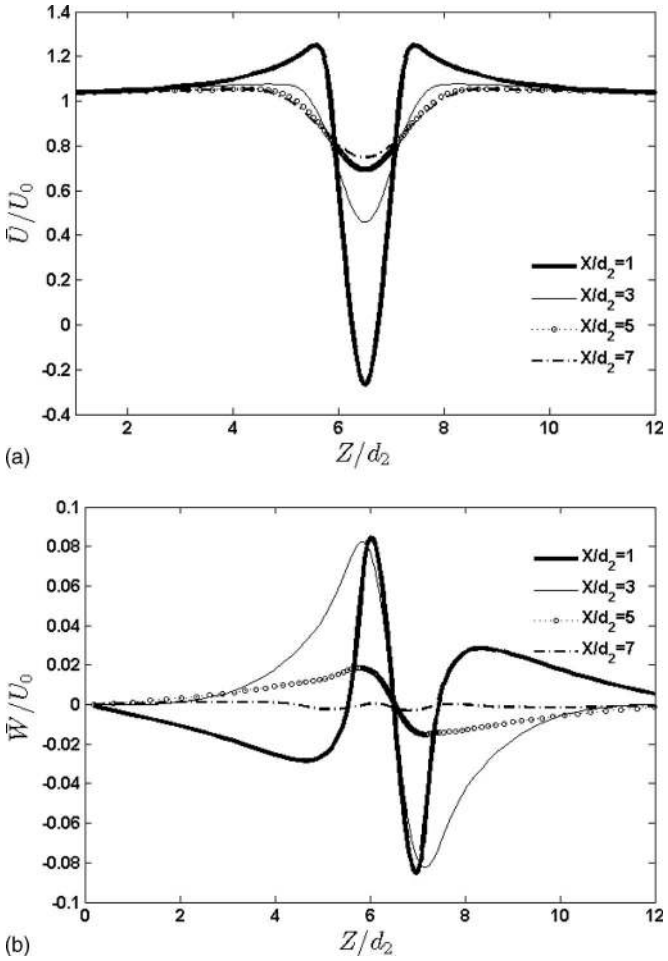

FIG. 9. Velocity profiles at some characteristic streamwise locations (X is measured from the plate). (a) Mean streamwise velocity $\bar{U}/U_0$; (b) mean cross-stream velocity $\bar{W}/U_0$; $\mathrm{Re}_{dm}=62.5$.

B. Reynolds-averaged statistics

The self-preservation principle which makes the far wake self-similar does not hold in the near wake. Turbulent wake flows are routinely described by means of Reynolds-averaged quantities, notably the mean flow and the Reynolds stresses, i.e., first and second velocity moments. A Reynolds decomposition in which the instantaneous velocity field is separated into mean and fluctuating parts can also be used for unsteady wakes. However, the unsteadiness results from vortex dynamics rather than turbulence. In this section, profiles of the primary velocity statistics at midspan ($\mathrm{Re}_{\mathrm{local}}=62.5$) are shown in Figs. 9 and 10 for the mean velocity components and the Reynolds-stress components, respectively. Mean values are obtained by averaging in time and the time averages are identified by an overbar.

The variation of the mean streamwise velocity component $\bar{U}$ in Fig. 9(a) shows that the velocity defects in the near wake decrease monotonically with the downstream distance X/d_2 from the plate. The maximum velocity defect is naturally found at the midplane $Z/d_2=6.5$. Due to the blockage of the plate, a considerable velocity overshoot of about 25% just outside the wake is observed at $X/d_2=1.0$. The profiles of the cross-stream mean velocity component $\bar{W}$ in Fig. 9(b)

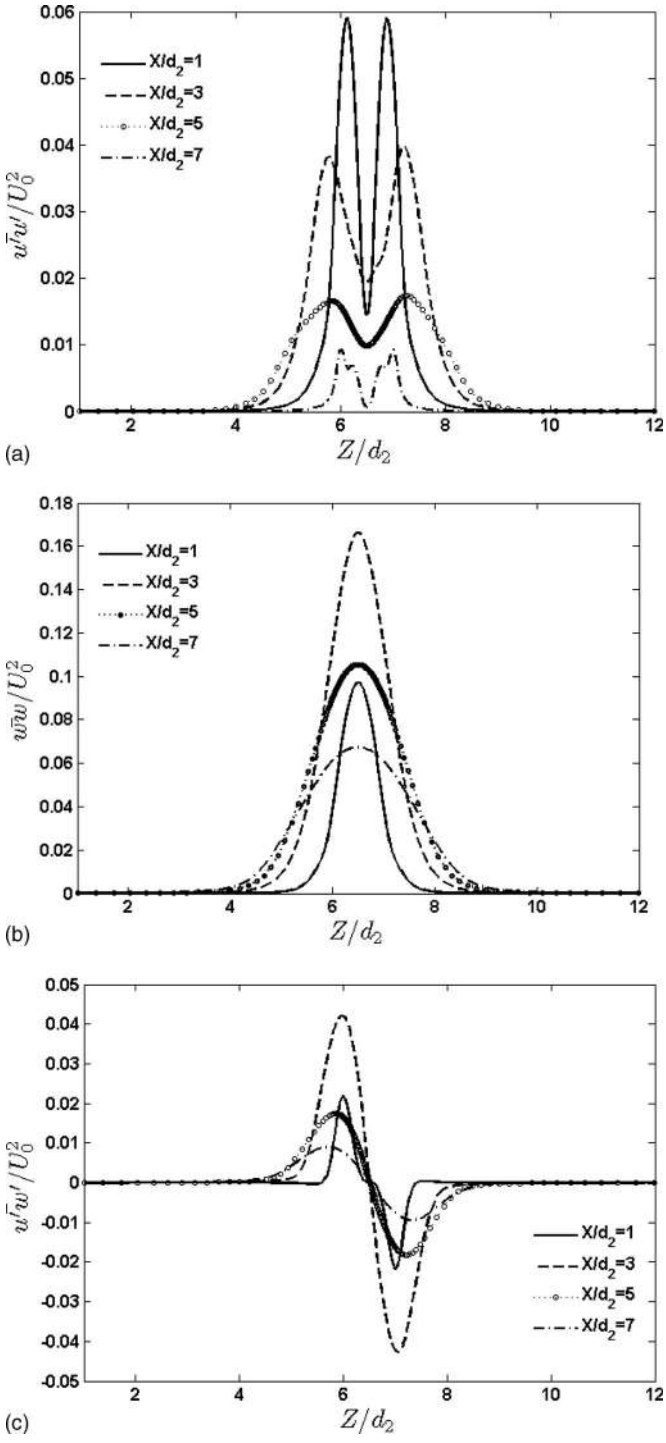

FIG. 10. Reynolds-stress profiles at the same streamwise locations as in Fig. 9. (a) Streamwise component $\overline{u'u'}/U_0^2$; (b) cross-stream component $\overline{w'w'}/U_0^2$; (c) shear- stress $\overline{u'w'}/U_0^2$, all at $\mathrm{Re}_{dm}=62.5$.

exhibit an antisymmetric variation about the midplane $Z/d_2=6.5$. Outside the very near wake at $X/d_2=1.0$ the mean velocity vector is directed away from the X axis, $\bar{W}<0$ for $Z/d_2<5.0$ and $\bar{W}>0$ for $Z/d_2>8.0$. This suggests the existence of a recirculation bubble just downstream of the plate which tends to deflect the outer flow. Near the X axis, on the other hand, the cross-stream mean velocity is directed toward the X axis. At $X/d_2=3.0$ and further downstream, the cross-stream velocity $\bar{W}$ is consistently directed toward the X axis.

The bimodal $\overline{u'^2}$ profiles in Fig. 10(a) closely resemble those observed in the near wake of a uniform circular cylinder by Persillon and Braza.[29] The highest levels of streamwise velocity fluctuations are found in the shear layers shed from the tapered plate and hence two distinct $\overline{u'^2}$ peaks are offset from the wake centerline. The cross-stream velocity fluctuations $\overline{w'^2}$, however, attain their highest level along the wake centerline. Due to symmetry the alternating vortices shed from either side of the plate contributes equally. It is noteworthy that $\overline{w'^2}$ increases with X in the very near wake and reaches an absolute maximum near $X/d_2=3$ and thereafter gradually decreases further downstream. The cross-stream velocity fluctuations are generally more energetic than the streamwise velocity fluctuations throughout the wake region. The cross correlation $\overline{u'w'}$ in Fig. 10(c) exhibits an antisymmetrical variation across the wake at all downstream locations. The peaks in the $\overline{u'w'}$ distributions show where the streamwise fluctuations are mostly correlated with the cross-stream velocity fluctuations. The positive peak, for instance, stems from the anticlockwise vortices shed from the lower edge of the plate at $Z/d_2=6$.

C. Secondary motion and formation length

Secondary motions in the unsteady laminar wake and in the front stagnation zone of the tapered plate arise primarily due to the tapering and tend to enhance the complexity of the overall flow pattern. In the front stagnation zone of the plate, the spanwise mean velocity component $\bar{V}$ in Fig. 11(a) is consistently positive and the secondary flow is thus directed from the wide end of the plate toward the narrow end. The isobars in Fig. 12(a) moreover show that this motion, typically of the order of $0.05U_0$ at midspan, is pressure driven.

On the lee side of the plate, Gaster and Ponsford[11] (TR=18) and Narasimhamurthy *et al.*[5] (TR=20) observed a rather complex flow pattern. Gaster and Ponsford[11] in their high-Reynolds-number *turbulent* flow noticed a stream from the wide end of the plate toward the narrow end in the downstream vicinity of plate. This stream was also detected next to the plate by Narasimhamurthy *et al.*[5] Slightly further downstream, however, they discovered an oppositely directed flow, i.e., from the narrow end toward the wide end of the plate, driven by pressure differences. In the current simulation of unsteady *laminar* flow, the secondary motion downstream of the plate is somewhat different from the flow patterns observed in the turbulent flow regime.[5,11] The streamwise and spanwise variations of $\bar{V}$ shown in Figs. 11(b) and 11(c), respectively, show that the secondary motion goes from the wide end toward midspan in the wake behind the wider part of the plate. In the near wake behind the narrow end of the plate, the secondary spanwise motion is mostly directed toward the wider end ($\bar{V}<0$) and this motion persists roughly over $\frac{3}{4}$ of the plate length. At the narrow end where no vortex shedding occurs, modest positive $\bar{V}$ values can be observed in the immediate vicinity of the plate (i.e., $X/d_2=5.025$ and $X/d_2=5.10$). This change in

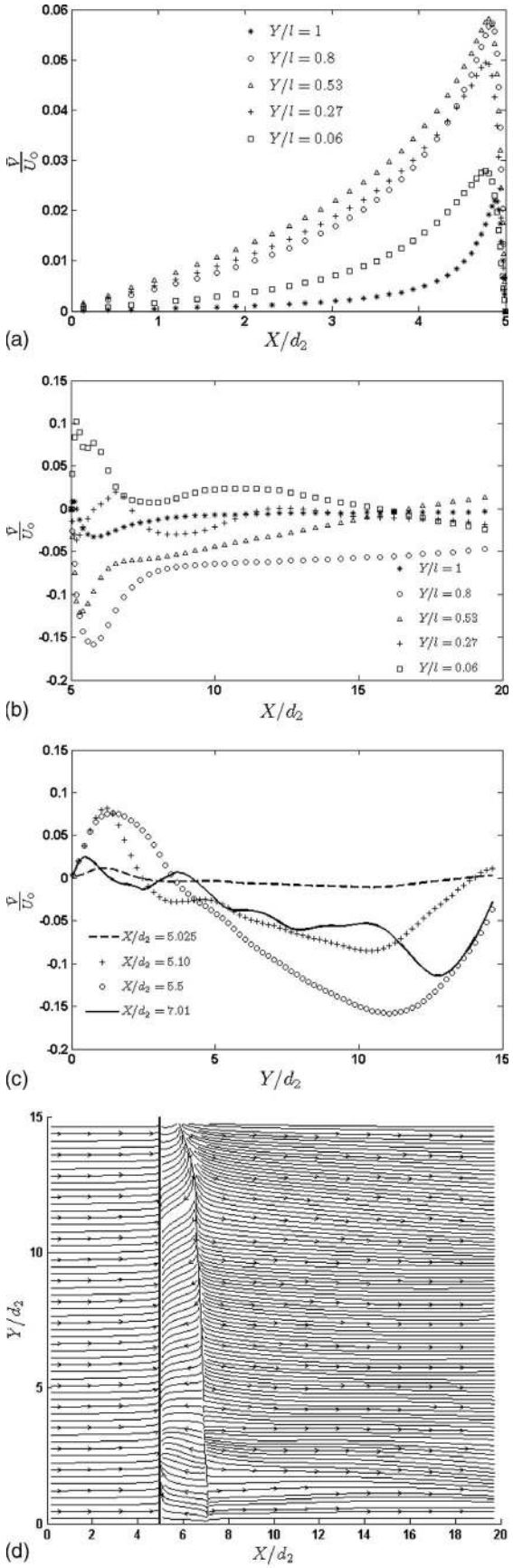

FIG. 11. Time-averaged spanwise velocity (secondary flow) at different spanwise locations. (a) Upstream of the plate; (b) downstream of the plate; (c) downstream of the plate vs Y/d_2 for different x positions; (d) stream trace of the time-averaged velocity. All data are from the midsection (i.e., Z/d_2=6.5).

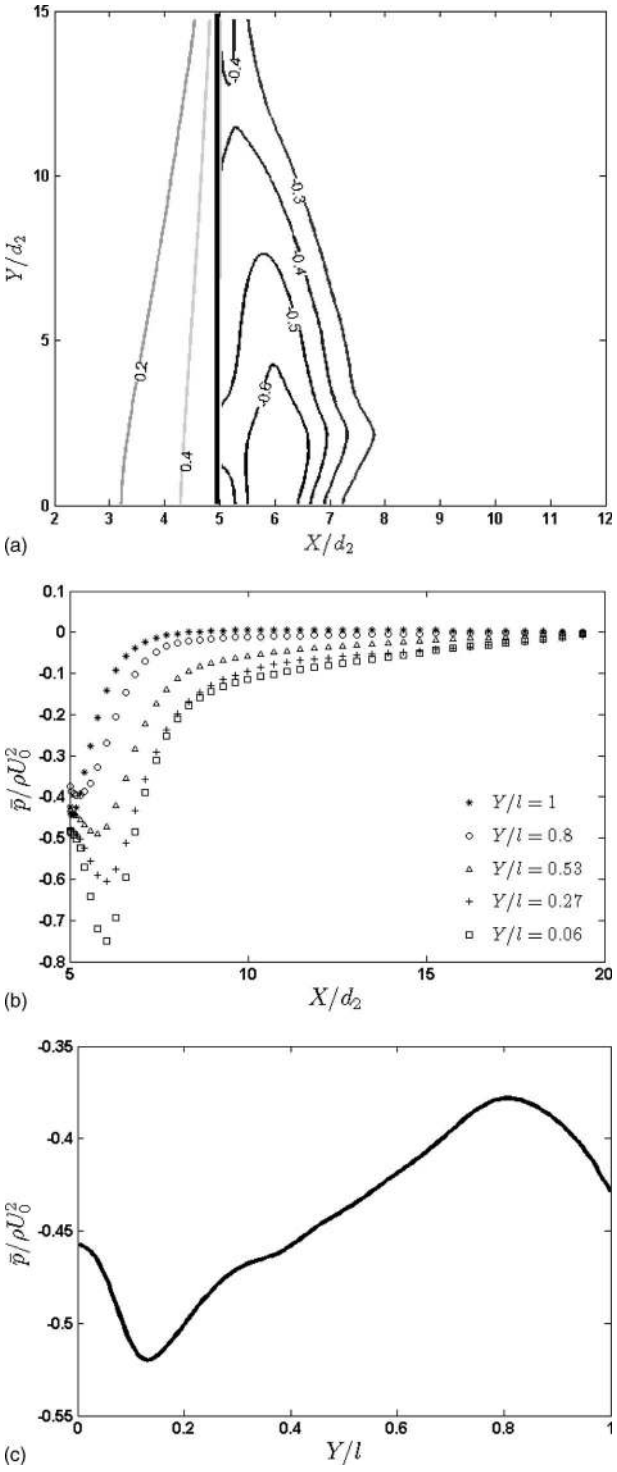

FIG. 12. (a) Isocontours of the mean pressure $\bar{p}/\rho U_0^2$ in the X-Y plane through the axis of the plate. The data are from the midsection (i.e., Z/d_2=6.5). (b) Downstream variation of the normalized mean pressure downstream of the plate. (c) Spanwise variation of the normalized mean pressure at the midsection Z/d_2=6.5 of the plate (base pressure).

sign of $\bar{V}$ shows that the secondary flow is locally redirected within this tiny area. An overall impression of the secondary flow field in the geometrical midplane is provided by Fig. 11(d).

The contour plot in Fig. 12(a) shows the topology of the mean pressure field $\bar{P}$ in the symmetry plane. While $\bar{P}$ is

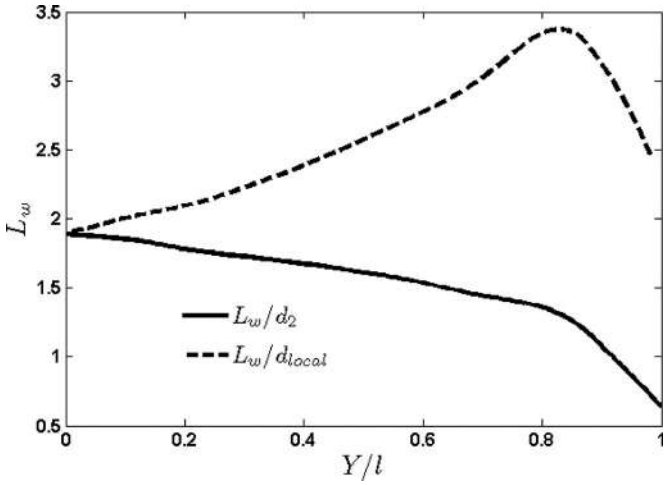

FIG. 13. Spanwise variation of the formation length of the wake of the tapered plate normalized by d_2 and d_{local}, respectively.

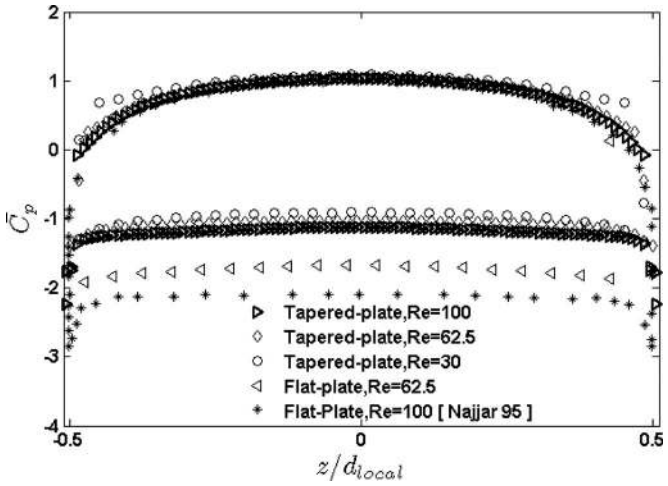

FIG. 15. Mean pressure coefficient for different cases at different Reynolds numbers. Here z denotes the position on the plate measured from the centerline, i.e., $z=z-z_{\text{middle}}$.

positive upstream of the plate, $\bar{P}$ is negative everywhere downstream of the plate with a minimum value below $-0.60\rho U_0^2$ about $X/d_2=6$, i.e., $1d_2$ away from the plate. The streamwise variation of $\bar{P}$ in the wake region is shown in Fig. 12(b) whereas the spanwise variation of the base pressure is presented in Fig. 12(c). The highest base pressure on the plate is about $-0.375\rho U_0^2$ and is observed at $Y/d_2 \approx 12$. The secondary mean flow $\bar{V}$ is believed to be driven by the spanwise pressure gradient associated with the base pressure variation. Narasimhamurthy *et al.*[5] recently arrived at an analogous conclusion regarding the primary driving mechanism in the turbulent flow regime.

The spanwise variation of the nondimensional length of the mean recirculation zone is shown in Fig. 13. This so-called formation length L_w is defined as the streamwise extent of the closed wake (recirculation region) which results after time averaging of the velocity field. Figure 14 shows an isocontour plot of the time-averaged streamwise velocity $\bar{U}$.

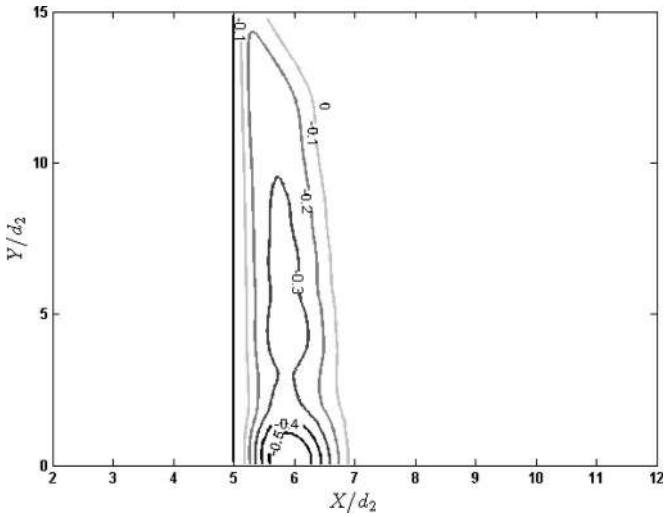

FIG. 14. Isocontour plot of the time-averaged normalized streamwise velocity depicting the region of recirculation. Data from the midsection (i.e., $z/d_2=6.5$).

The zero-contour represents the border between flow in the streamwise and upstream directions and envelops the separation bubble. This particular contour line corresponds to the solid line for L_w/d_2 in Fig. 13. The broken line in Fig. 13 shows that also L_w/d_{local} varies substantially along the span, from about 1.9 at the wide end and up to a maximum close to 3.4 at $Y/d_2 \approx 13$ near the narrow end. At midspan $L_w/d_{\text{local}} \approx 2.6$, whereas $L_w/d \approx 1.527$ in the present parallel-sided plate (see Table II). This observation is consistent with the recent findings by Narasimhamurthy *et al.*[5] from their simulations of turbulent wake flows. They reported that the formation length in their tapered plate case was about three times larger than $L_w/d \approx 2$ found by Najjar and Vanka[2] for a nontapered plate at Re=1 000. This is in agreement with earlier observations by Gaster and Ponsford[11] who also reported a shorter formation length and stronger vortex shedding in the wake behind a parallel-sided plate as compared to that of the tapered plate. On the basis of these observations Narasimhamurthy *et al.*[5] suggested a coupling between the formation length and strength of the vortex shedding. The more coherent and intense vortex shedding behind a uniform plate reduces the formation length. Recalling the local Strouhal number of 0.1414 at midspan of the tapered plate (see Table III) and the substantially higher St=0.1704 found for the parallel-sided plate demonstrates that a similar coupling between L_w and the vortex shedding exists also in the present laminar wake.

D. Mean pressure coefficient

The variation of the mean pressure coefficient defined as $\bar{C}_p \equiv 2(\bar{P}-P_0)/(\rho U_0^2)$ across the plate is shown in Fig. 15. Here, the reference pressure P_0 is taken as the inflow pressure. The cross-stream coordinate is measured from the centerline of the plate and scaled with the local width d_{local} of the plate. With this scaling the $\bar{C}_p$ distributions across the tapered plate nearly collapse irrespective of the actual local plate width. Results from the present parallel-sided plate simulation at Re=62.5 and the earlier results reported by

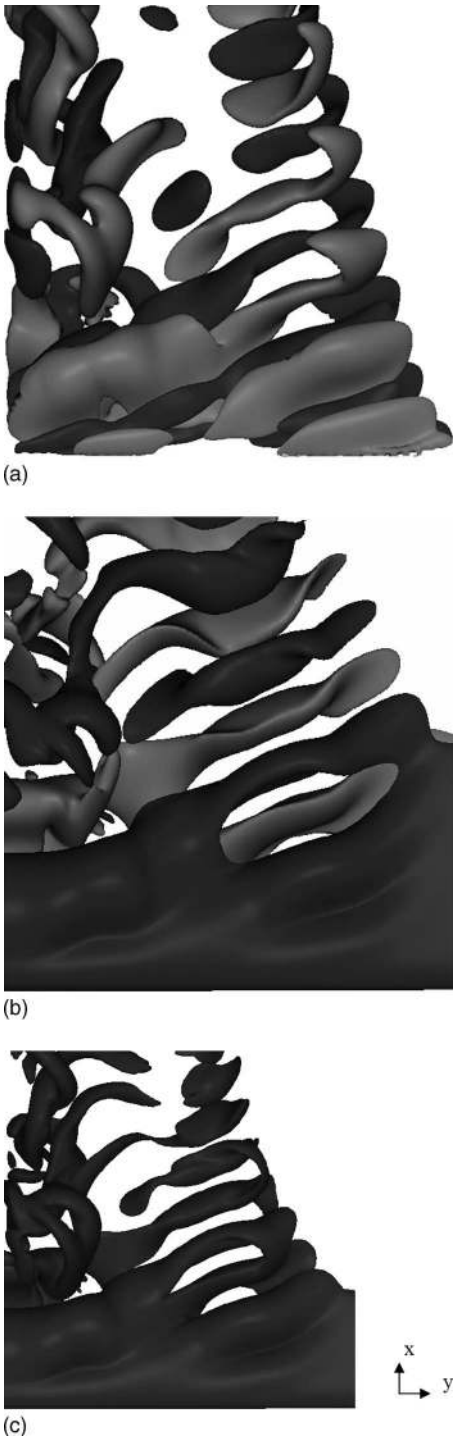

FIG. 16. (a) 3D isosurface plot of streamwise vorticity at time $t=360d_2/U_0$. The plate is at the bottom of these figures with the wide end to the left and the flow is upwards. White: $\omega_x\nu/U_0^2=-0.004$; black: $\omega_x\nu/U_0^2=+0.004$. (b) Spanwise vorticity, otherwise as in (a). (c) Vorticity magnitude $|\omega|\nu^2/U_0^4=5e-5$, otherwise as in (a).

Najjar and Vanka[18] at Re=100 are also included. The pressure variations along the front side of the plate are nearly indistinguishable, except close to the narrow end of the tapered plate (Re=30) where no vortex shedding takes place. While the base pressure variation is only modestly dependent on the local Reynolds number for the tapered plate, $\bar{C}_p$ is substantially lower in the uniform plate simulations.[5,18] The

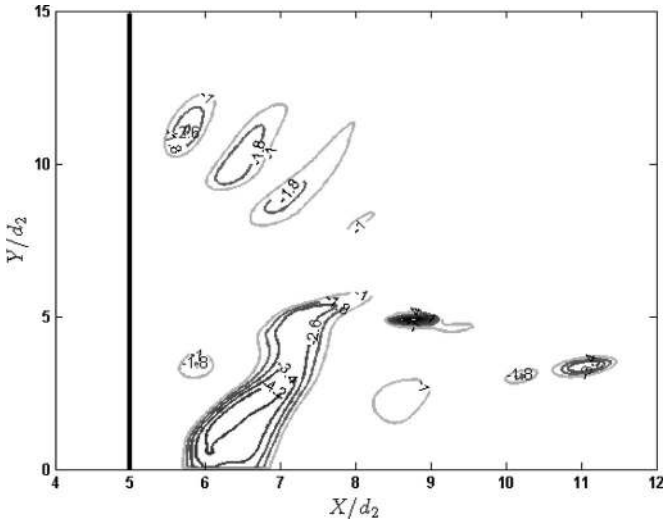

FIG. 17. Isocontour plot of λ_2 in the midsection of the domain. The bold line identifies the tapered plate.

somewhat lower base pressure $\bar{C}_p$ found by Najjar and Vanka[18] than by Narasimhamurthy *et al.*[5] could be due to a Reynolds number effect. It is noteworthy that irrespective of the local Reynolds number the base pressure coefficient is consistently higher for the tapered plate case than behind a parallel-sided plate.

E. Instantaneous vortical structures

In an attempt to better understand the dynamics of the vortex structures in the laminar wake of a tapered plate, the instantaneous flow field and the accompanying vorticity will be explored in this section. The instantaneous vortex structures impact on the time-averaged mean values and thus in turn on macroscopic quantities such as the drag force. The streamwise and spanwise components of the vorticity vector, i.e., $\omega_x=\partial w/\partial y-\partial v/\partial z$ and $\omega_y=\partial u/\partial z-\partial w/\partial x$, are shown in Figs. 16(a) and 16(b) at $t=360\ d_2/U_0$, together with the magnitude of the instantaneous vorticity vector $|\omega|=1/2(\omega_x^2+\omega_y^2+\omega_z^2)$ in Fig. 16(c). The plate is at the bottom of the figures and it is immediately observed that three different vortex patterns exist. At the narrow end (to the right in these figures), no vortex shedding takes place simply because the local Reynolds number is too low. In the central region, a regular pattern of periodically shed vortical cells is evident. This regime of alternating vortices with positive and negative spanwise vorticities is most clearly seen in Fig. 16(b). The spanwise vorticity shed from the edges of the plate results in an inclined pattern of alternating but otherwise regular vortices. Downstream of the leftmost part of the plate, the regularity of the vortices is broken and a wriggling pattern of streamwise vorticity is observed. Here, the vorticity field consists of twisted and squirmed longitudinal vortex filaments and "slingshotlike" structures. The topology of the present vortex pattern does not suggest that any predistinguished modes (mode *A* or *B*; see, e.g., Ref. 1) of transition are present. The irregularity of the vortex shedding and the early breakdown of the Karman vortices into distorted longitudinal structures are probably due to secondary instabili-

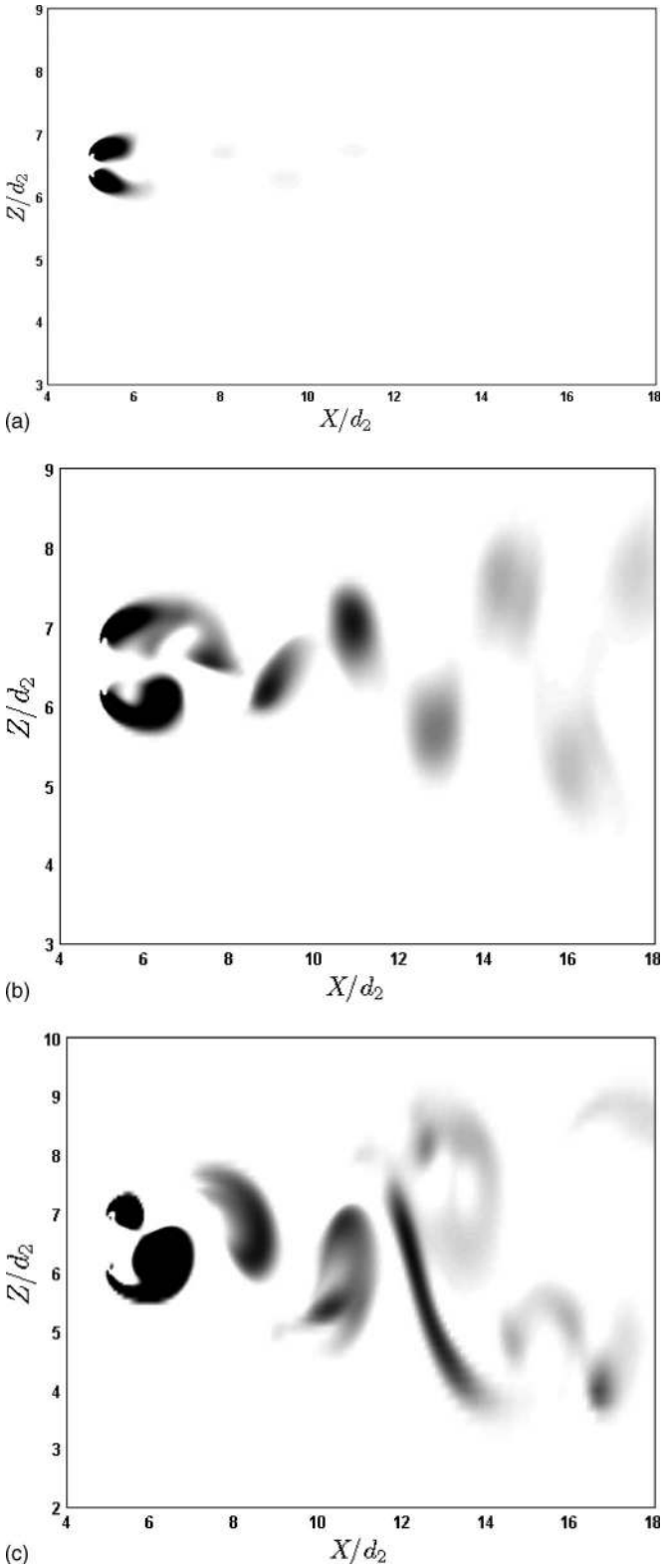

FIG. 18. Contour plots of λ_2 at three different spanwise locations: (a) $Re_{local}=30$; (b) $Re_{local}=62.5$, i.e., midspan; (c) $Re_{local}=95$.

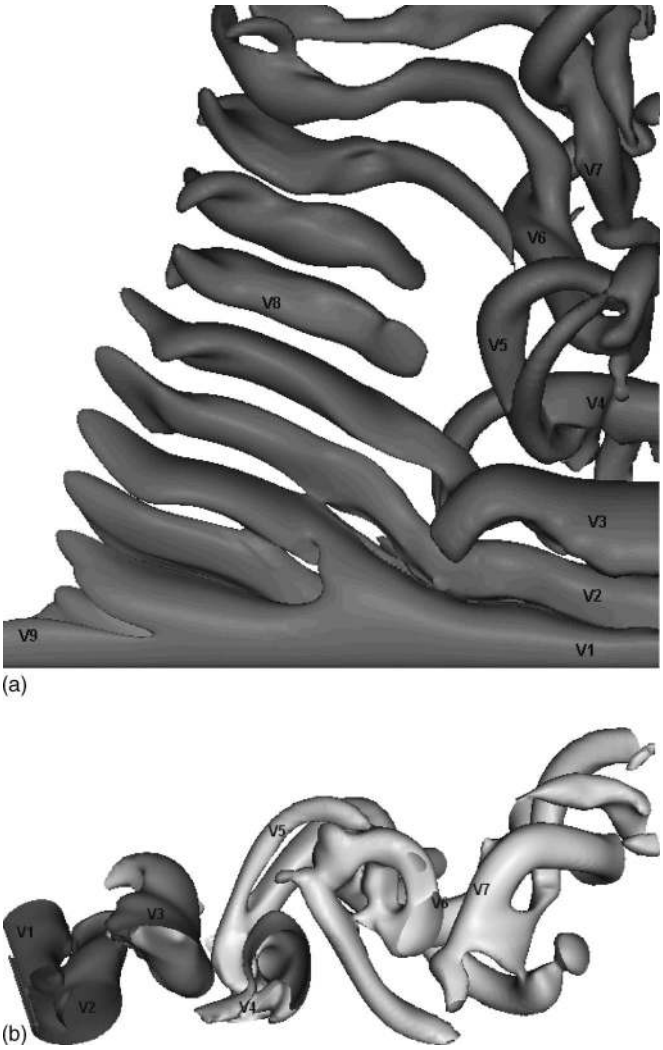

FIG. 19. Isosurface plots of $-\lambda_2$. (a) The plate is at the bottom of this figure with the wide end to the right and the flow is upwards. Notice that the plate is oriented differently than in Fig. 16 in order to show the slingshot structure V_5 downstream of the wide end. (b) Perspective view of $-\lambda_2$ downstream of the wider part of the plate.

ties which first produce localized regions of highly concentrated streamwise vorticity. When the spanwise Karman roller is shed from the plate, the vortex becomes distorted and takes the shape of elongated longitudinal structures which fork into two branches resembling the slingshot shape.

In order to visualize the topology of vortex cores the λ_2 definition proposed by Jeong and Hussain[30] is used. λ_2 corresponds to the second largest eigenvalue of the symmetric tensor $S_{ij}S_{ij}+\Omega_{ij}\Omega_{ij}$ where S_{ij} and Ω_{ij} represent the symmetric and antisymmetric parts of the velocity gradient tensor. Negative values of λ_2 are associated with low-pressure zones and vortex cores. A snapshot of negative isocontours λ_2 in the midplane is shown in Fig. 17. The oblique vortices shed from the narrower half of the plate die out as they are convected downstream. The strong vortex structures shed from the widest part of the plate break down into smaller yet rather intense longitudinal vortex elements. Figure 18 shows cross-stream contour plots of λ_2 at three spanwise locations which corresponds to three different local Reynolds numbers. The lowest negative λ_2 levels and thus the strongest vortices are associated with the darkest areas. The distinctly different flow regimes along the span are clearly visible. The cores of shedding vortices become gradually stronger toward the wider end of the plate, i.e., as Re_{local} increases. The most

distinct and regular vortex street is observed at midspan where a series of alternating vortices persists throughout the computation domain, i.e., $15d_2$ downstream of the plate.

The 3D isosurface of λ_2 in Fig. 19(a) reveals an almost identical vortex pattern as that of the isosurface of the vorticity magnitude in Fig. 16(c). The three distinct flow regimes are observed also here: a steady state at the narrow end, regular oblique vortex shedding around midspan, and irregular and chaotic breakdown of spanwise vortices into longitudinal filaments at the wide end. Some distinct vortex cores are labeled as V_1-V_9. At the narrow end of the plate, where no shedding takes place, the conically shaped bubble is marked as V_9. The vortex denoted V_8 is one of the regular oblique shedding cells inclined with respect to the plate.

In the very near wake of the wide part of the plate, four slightly oblique but otherwise regular vortex rolls (V_1-V_4) can be observed. The same vortices are also visible in the perspective view of the wake topology in Fig. 19(b) where only the wake downstream of the wide side is shown. As the vortices are convected downstream, the regular vortex pattern breaks up and the vortex V_5 branches into two parts which resemble the shape of a slingshot. The two branches of V_5 appear as longitudinal structures above two vortex rollers (V_4 and V_6) and eventually come together downstream. The underlying mechanism for these complex phenomena is probably associated with a secondary instability which sets in when the local Reynolds number exceeds about 80. If so, it is likely that this instability is triggered by the inherent three dimensionality due to the tapering of the plate.

IV. CONCLUDING REMARKS

The present study has been concerned with the unsteady laminar wake behind a tapered plate. This flow configuration has been studied rather extensively before but only for other Reynolds number ranges. The wake topology in the present low-Reynolds-number range exhibited a surprising complexity downstream of the wide end of the plate where streamwise-oriented vortex structures occurred as the result of an unexpected three dimensionalization of the regular oblique shedding pattern at midspan. A particularly fascinating feature of this special wake flow is the coexistence of three different flow regimes literally side by side in the same configuration. In addition, the cellular vortex shedding and oblique vortex structures were observed behind a tapered plate in this numerical experiment. Frequency analysis and 3D visualization collectively confirmed that multiple cells of constant shedding frequency exist along the span of the plate.

The present 3D simulation revealed a pressure-driven spanwise secondary motion. It was shown that in the front stagnation zone the secondary flow goes from the wide end of the plate toward the narrow end. The secondary flow in the downstream of the plate is more complex though.

Comparisons with results for wake flow behind a uniform plate at the same Reynolds number showed that the tapering gave rise to a lower Strouhal number and a significantly higher base pressure. The latter finding implies that the pressure drag is reduced due to the tapering.

ACKNOWLEDGMENTS

The authors are grateful to the Research Council of Norway for a grant of computation time (Programme for Supercomputing). The first and second authors are thankful to the Research Council of Norway for their financial support. The constructive comments of the anonymous reviewers are appreciated.

[1] C. H. K. Williamson, "Vortex dynamics in the cylinder wake," Annu. Rev. Fluid Mech. **28**, 477 (1996).
[2] F. M. Najjar and S. P. Vanka, "Effects of intrinsic three-dimensionality on the drag characteristics of a normal flat plate," Phys. Fluids **7**, 2516 (1995).
[3] M. Gaster, "Vortex shedding from slender cones at low Reynolds numbers," J. Fluid Mech. **38**, 565 (1969).
[4] P. S. Piccirillo and C. W. Van Atta, "An experimental study of vortex shedding behind linearly tapered cylinders at low Reynolds number," J. Fluid Mech. **246**, 163 (1993).
[5] V. D. Narasimhamurthy, H. I. Andersson, and B. Pettersen, "Cellular vortex shedding in the wake of a tapered plate," J. Fluid Mech. **617**, 355 (2008).
[6] D. J. Maull and R. A. Young, "Vortex shedding from bluff bodies in shear flow," J. Fluid Mech. **60**, 401 (1973).
[7] P. Parnaudeau, D. Heitz, E. Lamballais, and J.-H. Silvestrini, "Direct numerical simulations of vortex shedding behind cylinders with spanwise linear nonuniformity," J. Turbul. **8**, (2007).
[8] M. Gaster, "Vortex shedding from circular cylinders at low Reynolds numbers," J. Fluid Mech. **46**, 749 (1971).
[9] C. H. K. Williamson, "Oblique and parallel modes of vortex shedding in the wake of a circular cylinder at low Reynolds numbers," J. Fluid Mech. **206**, 579 (1989).
[10] D. Gerich and H. Eckelmann, "Influence of end plates and free ends on the shedding frequency of circular cylinders," J. Fluid Mech. **122**, 109 (1982).
[11] M. Gaster and P. J. Ponsford, "The flows over tapered plates normal to the stream," Aeronaut. J. **88**, 206 (1984).
[12] I. P. Castro and P. Rogers, "Vortex shedding from tapered plates," Exp. Fluids **33**, 66 (2002).
[13] I. P. Castro and L. Watson, "Vortex shedding from tapered, triangular plates: Taper and aspect ratio effects," Exp. Fluids **37**, 159 (2004).
[14] A. Fage and F. C. Johansen, "On the flow of air behind an inclined flat plate of infinite span," Proc. R. Soc. **116**, 170 (1927).
[15] A. E. Perry and T. R. Steiner, "Large scale vortex structures in turbulent wakes behind bluff bodies," J. Fluid Mech. **174**, 233 (1987).
[16] I. P. Castro and J. M. Jones, "Studies in numerical computations of recirculating flows," Int. J. Numer. Methods Fluids **7**, 793 (1987).
[17] D. S. Joshi, "Numerical studies of the wake of a plate normal to a free stream," Ph.D. thesis, University of Illinois at Urbana-Champaign, 1993.
[18] F. M. Najjar and S. P. Vanka, "Simulation of the unsteady separated flow past a normal flat plate," Int. J. Numer. Methods Fluids **21**, 525 (1995).
[19] F. M. Najjar, "Direct numerical simulations of separated and separated-reattaching flows on massively parallel processing computers," Ph.D. thesis, University of Illinois at Urbana-Champaign, 1994.
[20] S. Balachandar, R. Mittal, and F. M. Najjar, "Properties of the mean recirculation region in the wakes of two-dimensional bluff bodies," J. Fluid Mech. **351**, 167 (1997).
[21] F. M. Najjar and S. Balachandar, "Low frequency unsteadiness in the wake of a normal flat plate," J. Fluid Mech. **370**, 101 (1998).
[22] S. J. Wu, J. J. Miau, C. C. Hu, and J. H. Chou, "On low-frequency modulations and three-dimensionality in vortex shedding behind a normal plate," J. Fluid Mech. **526**, 117 (2005).
[23] M. Manhart, "A zonal grid algorithm for DNS of turbulent boundary layers," Comput. Fluids **33**, 435 (2004).
[24] R. Mittal and G. Iaccarino, "Immersed boundary methods," Annu. Rev. Fluid Mech. **37**, 239 (2005).
[25] N. Peller, A. Le Duc, F. Tremblay, and M. Manhart, "High-order stable interpolations for immersed boundary methods," Int. J. Numer. Methods Fluids **52**, 1175 (2006).
[26] C. H. K. Williamson, "The natural and forced formation of spot-like dislocations in the transition of a wake," J. Fluid Mech. **243**, 393 (1992).

[27]H. R. Tamaddon-Jahromi, P. Townsend, and M. F. Webster, "Unsteady viscous flow past a flat plate orthogonal to the flow," Comput. Fluids **23**, 433 (1994).
[28]A. K. Saha, "Far-wake characteristics of two-dimensional flow past a normal flat plate," Phys. Fluids **19**, 128110 (2007).
[29]H. Persillon and M. Braza, "Physical analysis of the transition to turbulence in the wake of a circular cylinder by three-dimensional Navier-Stokes simulation," J. Fluid Mech. **365**, 23 (1998).
[30]J. Jeong and F. Hussain, "On the identification of a vortex," J. Fluid Mech. **285**, 69 (1995).